

Addition of MgO Nanoparticles to Carbon Structural Steel and the Effect on Inclusion Characteristics and Microstructure



XIANGZHOU GAO, SHUFENG YANG, JINGSHE LI, HANG LIAO, WEI GAO,
and TUO WU

An innovative approach for pre-dispersing MgO nanoparticles with AlSi alloy nanoparticles was established, and the nanoparticles were dispersed well in carbon structural steel. After adding different mass fractions of MgO nanoparticles in steel, the majority of inclusions contained MgO-Al₂O₃ spinel and MgO-Al₂O₃-bearing hybrid inclusion, and these inclusions promoted acicular ferrite (AF) formation. With increasing amount of added nanoparticles, the average inclusion size increased from 0.90 to 1.50 μm and the inclusion size was considerably refined, but the ability of inclusions to induce AF was greatly declined. It was revealed that the inclusion size was the decisive factor influencing the inducing ability of inclusions for AF, which also got a solid support from the nucleation thermomechanical and dynamic analyses. When the mass fraction of MgO nanoparticles reached 0.05 pct, the proportion of AF in microstructure is relatively larger and the degree of interlocking of the AF within the microstructure was optimized. The ferrite grains also got refined and the average grain size decreased by more than 94 pct compared with that of the original steel.

DOI: 10.1007/s11663-015-0552-2

© The Minerals, Metals & Materials Society and ASM International 2015

I. INTRODUCTION

NOWADAYS, the demand for various kinds of steels with good mechanical properties, especially strength, plasticity, and toughness, is significantly increased. It is well known that fine-grained strengthening, one of the various strengthening processes, contributes to impeding dislocation movement of the internal microstructure when external forces are applied to steel materials. It is also the only method hitherto to simultaneously improve the above three mechanical properties. Fine-grained strengthening mainly focuses on inducing the precipitation of intragranular acicular ferrite (IAF) in austenite grains to improve the mechanical properties and service life of the materials.^[1] Conventionally, precipitation strengthening and thermomechanical processing are the most common methods to obtain appropriate microstructures.^[2,3] The latter can be achieved during actual production through austenite non-crystallization controlled rolling,^[4] strain-induced transformation, and accelerated cooling.^[5,6] However, the precise control of important

parameters such as micro-alloy content, cooling and rolling conditions must be specifically investigated in order to satisfy the individual requirements of different steels. Furthermore, with the thickness of the steel plates increasing continuously, larger welding energy must be input to maintain high fabrication efficiency, which ultimately would lead to microstructural coarsening in the heat-affected zone after welding.^[7] In recent years, one proposed theory named “grain refinement of steel by second-phase particles” may theoretically slide over the above defects.

The concept of incorporating second-phase particles in metal was first proposed by Zener.^[8] The main purpose of this concept is to retard austenite grain growth with the pinning effect of precipitates and develop fine AF structure. Initially, steel researchers tried controlling steelmaking conditions or adding certain alloy elements to steel melt to obtain small-sized second phases (less than or equal to 1 μm ^[9]) with thermally stable nature. This refinement mechanism is basically consistent with “oxide metallurgy” theory.^[10,11] Some studies^[12–14] demonstrate that Ti₂O₃ is the optimal species to provide active nucleation sites for AF when introduced into steel. Shang *et al.*^[15,16] also have performed a series of laboratory experiments to investigate the influence of steel composition, cooling velocity, and other relative factors on the inducing ability of titanium oxides for AF. High-melting titanium nitride (TiN) also can serve as the heterogeneous nuclei for inducing fine ferrite.^[17,18] Additionally, other studies have indicated that inclusions such as zirconium oxides, titanium, niobium, and vanadium carbonitrides, and cerium sulfides also could contribute to IAF

XIANGZHOU GAO, Ph.D. Candidate, SHUFENG YANG, Associate Professor, JINGSHE LI, Professor, HANG LIAO, WEI GAO, and TUO WU, Postgraduates, are with the State Key Laboratory of Advanced Metallurgy, University of Science and Technology Beijing, Beijing 100083, China and also with the School of Metallurgical and Ecological Engineering, University of Science and Technology Beijing, Beijing 100083, China. Contact e-mail: yangshufeng@ustb.edu.cn

Manuscript submitted May 26, 2015.

Article published online December 21, 2015.

Table I. Chemical Composition of Q235 Steel Used in This Study (Weight Percent)

C	Si	Mn	P	S	O
0.1550	0.1400	0.5900	0.0038	0.0017	0.0069

nucleation.^[19–23] The above-mentioned methods of obtaining second-phase particles belong to the Internal Precipitation Method (IPM). For IPM, the steelmaking process needs to be adjusted to decrease the precipitation temperature of the required particles, which demands higher requirements on liquid steel purity and the casting process such as the solidification, rolling, and heat treatment steps.^[24]

In 1978, Hasegawa *et al.*^[25] developed a spray dispersion technique to produce the first steel containing homogeneously dispersed fine zirconium dioxide particles which were sprayed from outside into the molten steel. This method can be called the external adding method (EAM). Gregg *et al.*^[26] also designed a technique for making steel samples with controlled contents of powdered mineral phases and proposed that titanium oxide particles were most efficient in nucleating AF. Some researchers^[27,28] have carried out many similar studies and also obtained similar results. In contrast to IPM, EAM has no excessive requirements for steel melt purity and is easier to control. Moreover, by adding particles externally, they not only have an effective influence on primary austenite grain behavior, but also have beneficial effects during the subsequent rolling and heat treatment processes. For these reasons, EAM has several advantages compared with IPM. However, reports related to EAM, and particularly its application in actual production processes, are limited and problems remain pertaining to experimental design.

Magnesium oxide (MgO), a thermally stable inclusion in steel melt, tends to disperse well in steel melt due to the relatively weak affinity between individual particles, minor lattice misfit with ferrite, and other appropriate characteristics^[29] In this study, an innovative pre-dispersion approach for the addition of nanoparticles into a steel melt is designed. Q235 steel was selected as the test steel in carbon structure steels. The chemical composition of the steel is shown in Table I. The subjects of this study involved investigation of the following aspects: (i) the chemical reaction mechanism after the addition of nanoparticles; (ii) the influence of the amount of added MgO nanoparticles on inclusion characteristics, such as composition, size, and distribution; and (iii) the influence of different mass fractions of MgO nanoparticles on steel microstructure.

II. EXPERIMENTAL PROCEDURE

A. Material Preparation and Experimental Procedure

To ensure that the MgO nanoparticles (average particle size of 25 nm) were well dispersed before adding

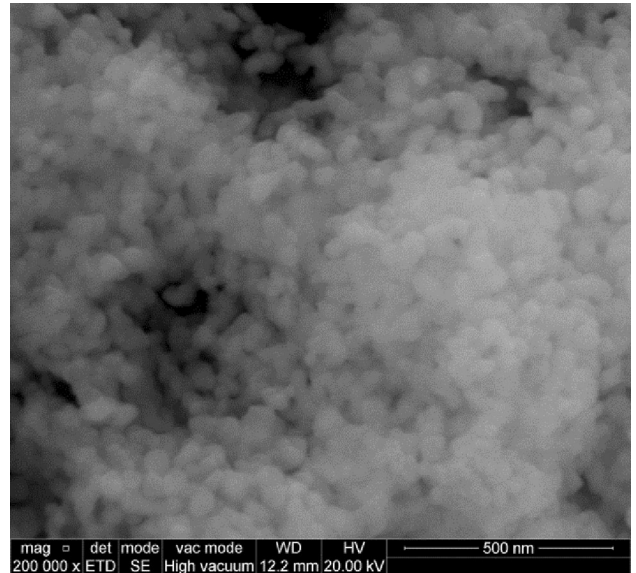


Fig. 1—Morphology of MgO nanoparticles (average particle size of 25 nm).

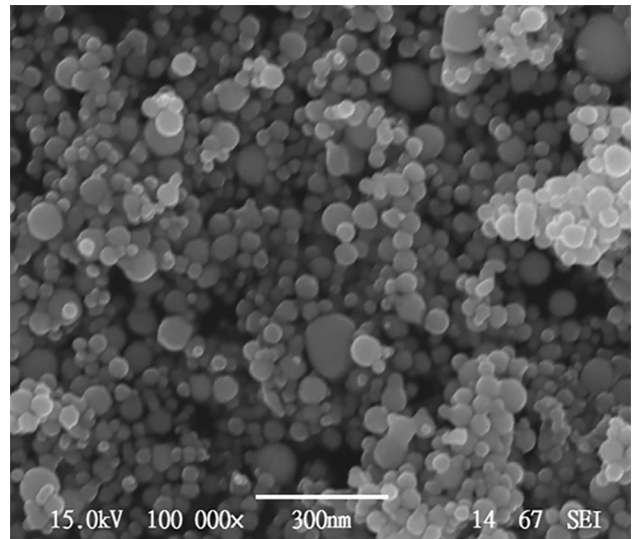


Fig. 2—Morphology of AlSi alloy nanoparticles (average particle size of 60 nm).

to the steel melt, another type of nanoparticle material, AlSi alloy (average particle size of 60 nm, Al-75 wt pct, Si-25 wt pct), was used as a pre-dispersion medium. Aluminum and silicon are the most common deoxidant elements used in steelmaking, so their addition would not cause contamination of the steel melt. The morphologies of MgO and AlSi alloy nanoparticles detected with scanning electron microscopy (SEM) are shown in Figures 1 and 2.

Figure 3 shows the flow diagram of the completed experimental process. The pre-dispersion process of MgO nanoparticles was performed using a planetary ball mill as shown in Figure 4 (IKN Mechanical Equipment Co., Ltd, Germany) with a weight ratio of MgO and AlSi alloy of 1:11. The rotation speed was

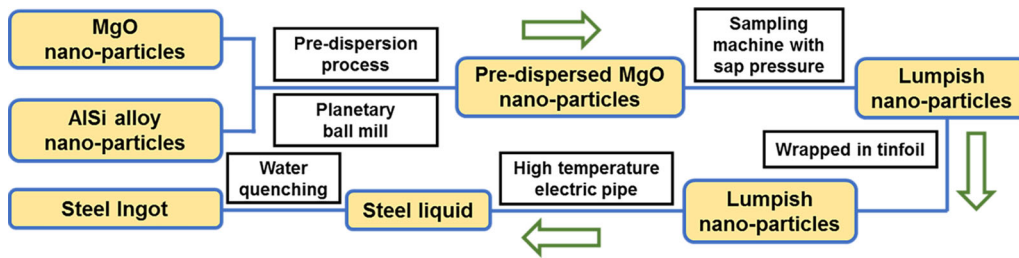


Fig. 3—Flow diagram of experimental procedure.

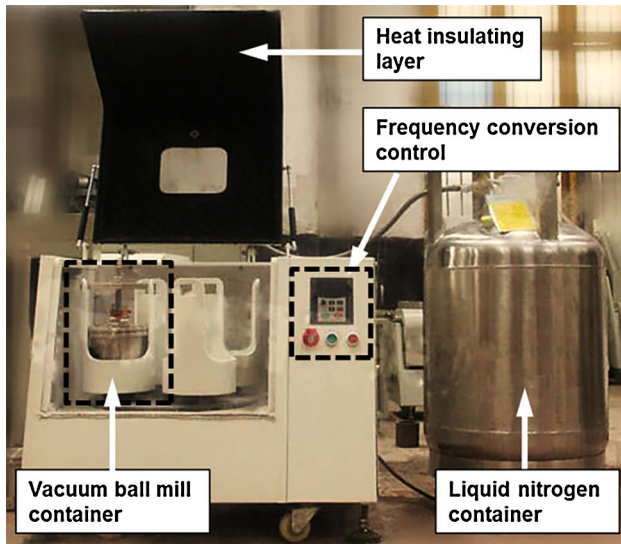


Fig. 4—Morphology of planetary ball mill equipped with liquid nitrogen cooling system.

maintained at 6000 rpm during the 3-hour process which was conducted under low-oxygen and low-temperature conditions to avoid the risk of high temperature arising from particle collisions. A sampling machine with sap pressure was then used to compact the pre-dispersed MgO nanoparticles into some blocks which were then wrapped individually in tinfoil. In each experimental group, about 300 g of Q235 remelting materials were melted in a high-temperature electric pipe furnace with an MoSi₂ heating element (Tianjin Taisite Instrument Co., Ltd, China). The furnace atmosphere was kept low in oxygen content on a constant inflow of purified argon gas, 100 L/h, from the bottom of the furnace. After the steel temperature reached 1873 K (1600 °C) and kept for 10 min at this temperature, a certain amount of pre-dispersed MgO nanoparticles were added to the steel melt. A molybdenum rod was used to stir the steel melt for 5 s every five minutes. After the stirring was repeated three times, the steel melt was maintained for 15 min and then solidification samples could be obtained by water quenching. The quenching process was performed in water at room temperature, i.e., 289 K (16 °C), and the cooling rate was about 45 K/s (45 °C/s). During this investigation, four different mass fractions of MgO nanoparticles, 0.02, 0.05, 0.1, and 0.3 pct, were evaluated during the laboratory experiments.

Table II shows the chemical composition of steel samples in different experimental groups. Selecting the case for the highest mass fraction addition of nanoparticles, 0.3 pct, the addition to the molten steel of aluminum from the Al-Si nanoparticle alloy and silicon from the Q235 remelting materials and Al-Si nanoparticle alloy, would increase the Al and Si contents of the steel by 2.344 and 0.755 pct, respectively. It also can be recognized from Table II that the majority of element Al exists in acid insoluble aluminum, so the additional acid-soluble aluminum would cause no obvious effects on the steel microstructure and the formation of AF. In general, the majority of element Si exists in acid-soluble silicon in steel and just a less amount silicon will participate in the formation of inclusions. It can be concluded from the previous research results^[30,31] that under the condition of rapid quenching, only high mass fraction of Si would have an obvious influence on the AF formation, so the influence of element Si on the steel microstructure can be neglected.

B. Detection Methods

1. Inclusion detection

Two cubic samples of 15 mm in side length were obtained from inside of each steel ingot. After mechanical grinding and polishing, about 100 typical inclusions selected randomly from each sample were examined with SEM and energy-dispersive spectrometry (EDS) to determine inclusion morphology, size, and type.

2. Microstructure observation

After etching the polished surface of steel samples with 4 pct Nital for 15 seconds, the steel microstructure as well as the three-dimensional morphology of inclusions was examined with the aid of a metallographic microscope and the SEM. The detailed making and treating processes of samples are shown in Figure 5.

III. RESULTS AND DISCUSSION

A. Inclusion Characteristics

The typical inclusion type in Q235 steel without the addition of MgO nanoparticles is shown in Figure 6. MnS inclusions (gray fraction) always formed on the surface of SiO₂ inclusions (black fraction), which is also in agreement with previous reports^[32] that sulfide inclusions generally precipitate on the surface of oxide

Table II. Chemical Compositions of Steel Samples with Different Addition Amounts of Nanoparticles (Weight Percent)

Experimental Groups	C	Si	Mn	P	S	O	Alt	Als
A	0.1550	0.1900	0.5900	0.0038	0.0017	0.0120	0.1590	0.0350
B	0.1550	0.2530	0.5900	0.0038	0.0017	0.0250	0.3990	0.0930
C	0.1550	0.4080	0.5900	0.0038	0.0017	0.0390	0.8550	0.1710
D	0.1550	0.8950	0.5900	0.0038	0.0017	0.1010	2.3440	0.5040

*A: 0.02 wt pct; B: 0.05 wt pct; C: 0.1 wt pct; D: 0.3 wt pct.

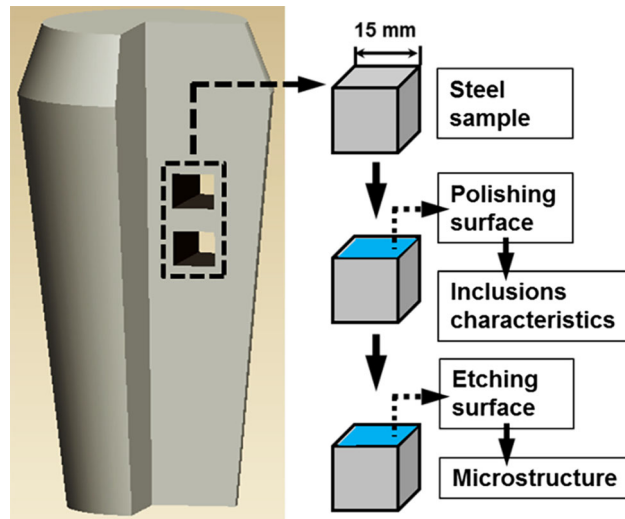


Fig. 5—Schematic diagram of the making and treating processes of steel samples.

inclusions. All of these inclusions were sphere like and the average size was 5 μm .

After adding MgO nanoparticles to steel melt, the main inclusion type varied with the addition of different amounts of nanoparticles as shown in Figure 7. When the mass fraction of MgO nanoparticles was 0.02 or 0.05 pct, the common inclusions in steel were MgO-Al₂O₃, MgO-Al₂O₃-MgS, and MgO-Al₂O₃-MgS-MnS hybrid inclusions, and the proportion of MgO-Al₂O₃ was obviously larger than that of the other two types of inclusions. When the mass fraction of MgO nanoparticles increased to 0.1 or 0.3 pct, the main inclusion type changed to MgO-Al₂O₃-MgS and MgO-Al₂O₃, and the proportion of the former was higher than that of the latter. It can be also concluded obviously from Figure 7 that the aggregation among inclusions tends to be serious with the addition of increasing amounts of MgO nanoparticles.

In order to confirm whether the MgO-Al₂O₃ inclusions belong to the magnesium aluminate spinel (MgO·Al₂O₃ spinel), all inclusions of this type under the addition of different amounts of nanoparticles were filtrated out and the weight percentage of MgO in MgO-Al₂O₃ inclusions was calculated. It was found from the statistical data that the maximum value of the weight percentage of MgO is less than 20 pct. Simultaneously, the MgO-Al₂O₃ binary phase diagram had been made using FactSage software based on the similar calculation method used in previous researches^[33–37] as shown in Figure 8. It can be concluded that under the

temperature of steel smelting, 1873 K (1600 °C), and within the distribution range of the weight percentage of MgO, the MgO-Al₂O₃ inclusions match the stoichiometric spinel composition (gray fraction shown in Figure 8). Namely, they belong to the type of MgO·Al₂O₃ spinel.

The distribution morphology of inclusions under the addition of different amounts of nanoparticles is shown in Figure 9. Virtually, all of the black spots indicated by the white arrows were examined to be MgO-Al₂O₃-bearing inclusions. It is obvious that with increasing amounts of MgO addition, the space between adjacent particles gradually decreases and the amount of inclusions per unit area gradually increases. In addition to that, the average size of inclusions also has an obvious increasing tendency.

A square domain with the area of 1 mm² was selected randomly from the observation surface of steel samples to measure the inclusion size, count the particle size distribution of inclusions, and add up the number of inclusions corresponding to the addition of different amounts of MgO nanoparticles. The particle size distribution histograms in Figure 10 show that when the mass fraction of MgO nanoparticles is 0.02, 0.05, and 0.1 pct, the MgO-Al₂O₃-bearing hybrid inclusions are relatively homogenous with a small distribution tail, and when the mass fraction increases to 0.3 pct, the concentration ratio of particle size distribution declines slightly. Figure 11 shows the variation tendency of average size and the number of inclusions with the addition of different amounts of MgO nanoparticles. With the addition of increasing amounts of MgO from 0.02 to 0.3 wt pct, the average inclusion size gradually increased from 0.90 to 1.50 μm , and the number of inclusions also increased gradually from 60 to 310. Compared with the average inclusion size of 5.0 μm in the initial steel sample, the results indicate that the average size of inclusions decreased by 82, 81, 77, and 70 pct, respectively.

B. Inducement of AF

Figure 12 shows the morphology of the AF induced by the inclusions with increasing mass fractions of MgO nanoparticles. All of the inclusions inducing AF were examined to be MgO·Al₂O₃ spinel or MgO-Al₂O₃-bearing hybrid inclusions.

When the mass fraction of MgO nanoparticles was at 0.02 and 0.05 pct, almost all of the induced ferrites were acicular like. Actually, each of the MgO-Al₂O₃-bearing hybrid inclusions could induce multiple strips of AF,

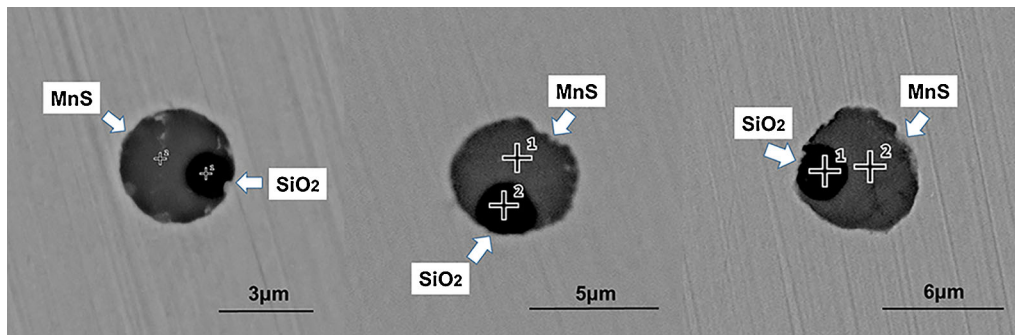


Fig. 6—Typical morphology and composition of inclusions in Q235 steel without the addition of nanoparticles.

and some of them could also pin on the prior austenite grain boundaries (PAGB) to retard the growth of the austenite grains. When the addition amounts of nanoparticles increased to 0.1 wt pct, the majority of ferrites induced by inclusions had block-like appearance and the average size of grains was relatively larger. With the addition of 0.3 wt pct MgO nanoparticles, the number of inclusions that could induce AF formation was further decreased and, in other words, the ability of inclusions to induce AF formation greatly declined.

C. Microstructural Characteristics

Figure 13 shows the microstructural evolution of steel samples with increasing mass fractions of MgO nanoparticles. For the Q235 steel with original composition, the microstructure consisted of coarse AF and pearlite (Figure 13(a)). With the addition of 0.02 wt pct MgO nanoparticles, some fine AFs appeared, distributed within the coarse ferrites which were still the primary microstructural feature (Figure 13(b)). With the addition of 0.05 wt pct MgO nanoparticles, fine AF became the primary constituent and other types of ferrites were rarely observed (Figure 13(c)). The AF crystals grew in different directions and improved the degree of interlocking. This type of microstructure hinders dislocation movement and reinforces the mechanical properties of the steel. However, when the mass fraction of the added MgO nanoparticles increased to 0.1 wt pct, large numbers of granular ferrites were generated and the proportion of AF also declined (Figure 13(d)). With the addition of 0.3 wt pct MgO nanoparticles, the microstructure was composed of massive coarse AF and sparse fine AF (Figure 13(e)). The microstructure morphology of these samples was similar to that of the steel samples without the addition of nanoparticles, but the average grain size of ferrites was obviously finer.

The average grain size in Figure 13 was counted by the metallography microscope equipped with an auto-statistic function as shown in Figure 14. The maximum value of grain size, 30.0 μm , was obtained in the steel without the addition of nanoparticles, and the minimum value, 1.7 μm , was obtained in the test steel with 0.05 wt pct MgO nanoparticles. The largest decrease was more than 94 pct. The decrease in the rate of grain size, 39, 65, and 43 pct, occurred during the

addition of 0.02, 0.10, and 0.30 wt pct MgO nanoparticles, respectively. From the analysis of these results, the optimal mass fraction of MgO nanoparticles is 0.05 pct.

IV. MECHANISTIC ANALYSIS

A. Inclusion Characteristics

In order to figure out the detailed precipitation behavior of inclusions during the solidification of Q235 steel melt with the addition of nanoparticles, the highest mass fraction of nanoparticles, 0.3 pct, was taken as an example to calculate the inclusion type and their relative content with FactSage software. As shown in Figure 15, the formed MgO-Al₂O₃ inclusions during the initial stage of experiment are MgO-Al₂O₃ spinel, which is in agreement with the previous conclusion from Figure 8. Based on the thermodynamic calculation results in Figure 15 and the experimental results described in Section III, a detailed schematic diagram of the inclusion precipitation behavior during the solidification of Q235 steel melt with the addition of nanoparticles is shown in Figure 16. Because the majority of element Si exists in acid-soluble silicon in steel and just a less amount silicon will participate in the formation of inclusions, the transition behavior of element Si is not included in Figure 16. When the MgO nanoparticles mixed with AlSi nanoparticles are added to the steel melt, they are quickly dispersed within the steel melt. MgO inclusions stay in the steel melt stably due to the property of thermal stability. The Al and Si dissolve in the steel melt quickly as shown in the third step of Figure 16. Due to the strong deoxidizing power of Al, it combines with dissolved oxygen to generate Al₂O₃ inclusions as shown in the fourth step of Figure 16. The strong stirring effect induced by the stirring of molybdenum rod facilitates the formation of MgO·Al₂O₃ spinel. As the steel temperature decreases below the precipitation temperature of sulfides, MnS and MgS inclusions begin to form on the surface of the oxide inclusions as shown in the fifth step of Figure 16, which is a common phenomenon in previous researches.^[38,39] However, due to that the percentage of sulfide phase in the hybrid inclusions is small and the size of the hybrid inclusions is also small, it is difficult to

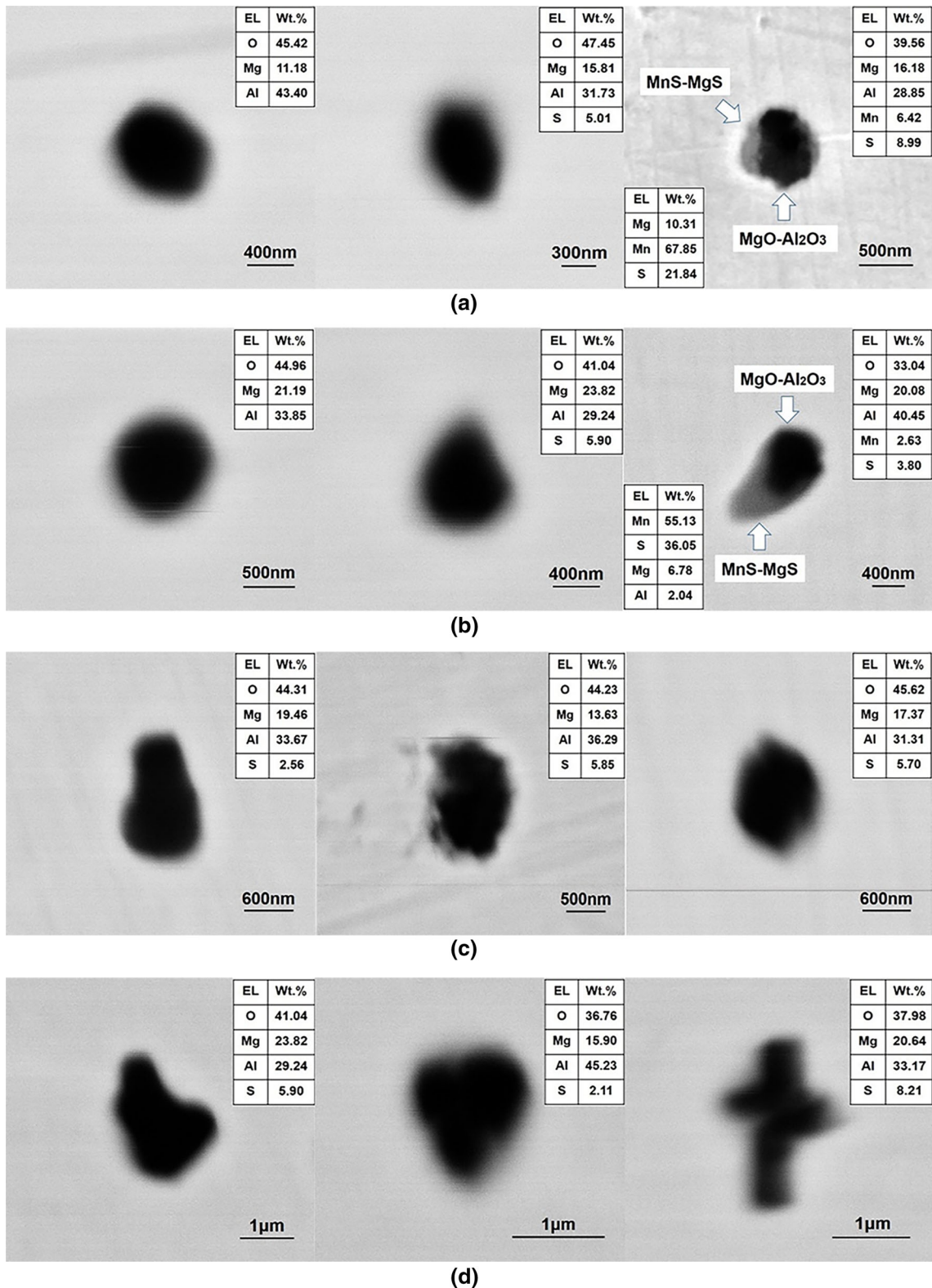


Fig. 7—Typical morphology and composition of inclusions in Q235 steel with the addition of different mass fractions of MgO nanoparticles: (a) 0.02 pct; (b) 0.05 pct; (c) 0.1 pct; and (d) 0.3 pct.

distinguish the duplex nature of the inclusions as shown in Figures 7 and 12.

As shown in Figure 11, the average size of inclusions increases with the increase in the amount of added

nanoparticles. This is mainly related to the different amounts of inclusions per unit volume (or per unit area) under different addition amounts of nanoparticles. With an increase in the number of nanoparticles in the steel

melt, the space between adjacent particles decreases and the probability of collision between adjacent particles will increase, which can be observed obviously in

Figure 9. This ultimately results in the aggregation and growth of particles.

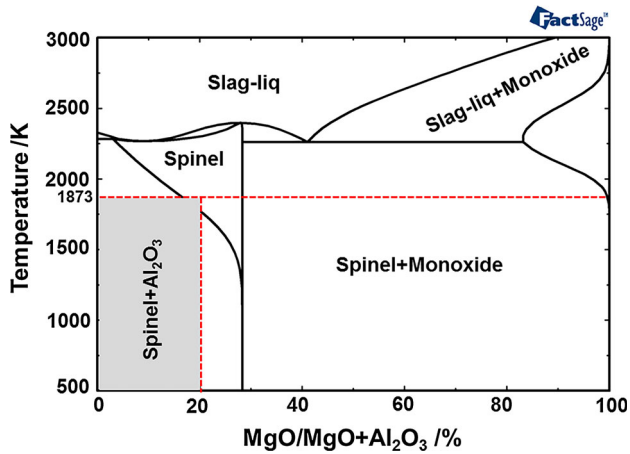


Fig. 8—Binary phase diagram of MgO-Al₂O₃.

B. Ferrite Nucleation

Although the initial purpose of this study is to apply MgO inclusions to induce AF and refine the steel microstructure, the generated MgO-Al₂O₃-bearing hybrid inclusions can play a similar role. The main factors that determine whether or not inclusions can act as nucleation cores to induce the generation of AF are inclusion type and size. In terms of nucleation mechanism of AF induced by MgO·Al₂O₃ spinel, Wen *et al.*^[40] have already conducted a relatively comprehensive analysis. The difference in the size of MgO·Al₂O₃ spinel formed in the initial stage of experiment directly influences the inducing abilities of MgO-Al₂O₃-bearing hybrid inclusions for AF formation as heterogeneous nuclei, which further affects the steel microstructure. Thus, the MgO-Al₂O₃ spinel size was the ultimate factor to determine the refining effect of steel microstructure.

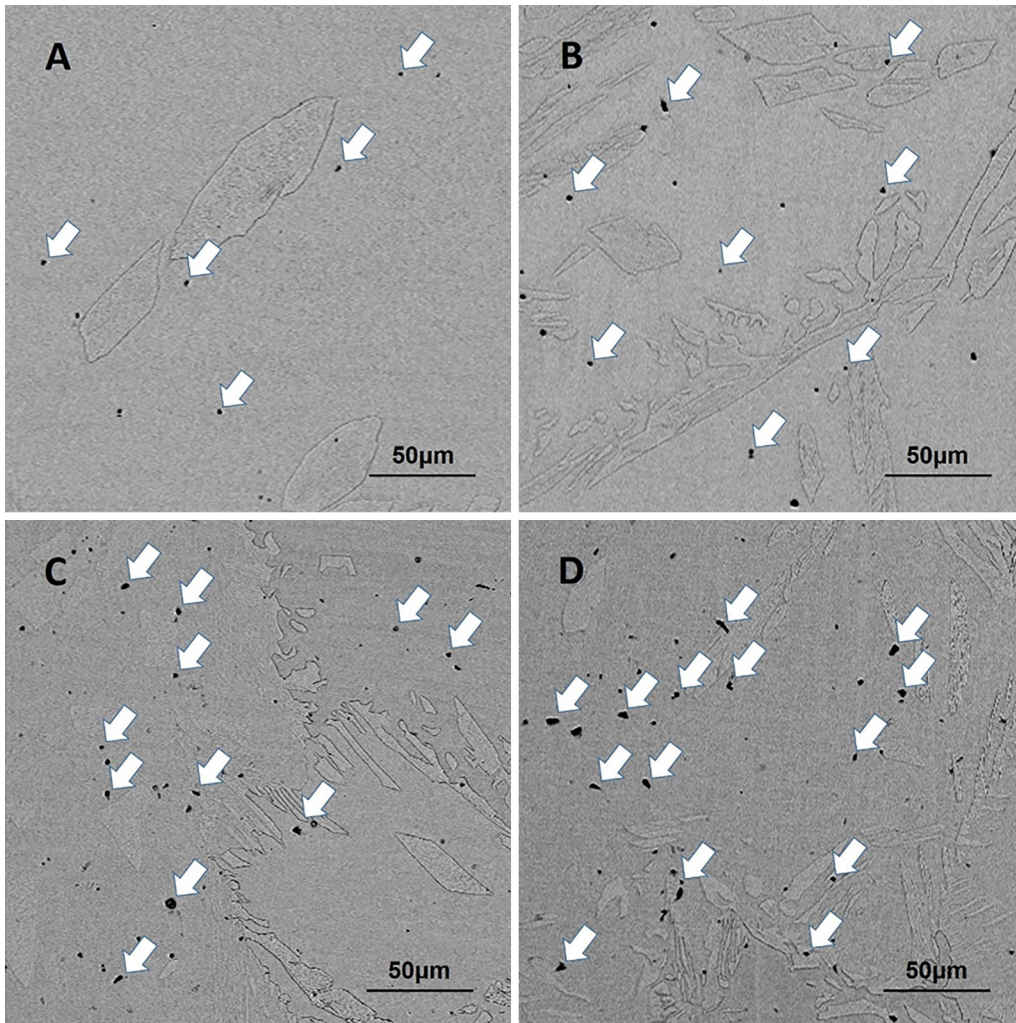


Fig. 9—Distribution morphology of inclusions under the addition of different amounts of MgO nanoparticles and same observation magnification ($\times 400$) with SEM: (a) 0.02 wt pct; (b) 0.05 wt pct; (c) 0.1 wt pct; and (d) 0.3 wt pct.

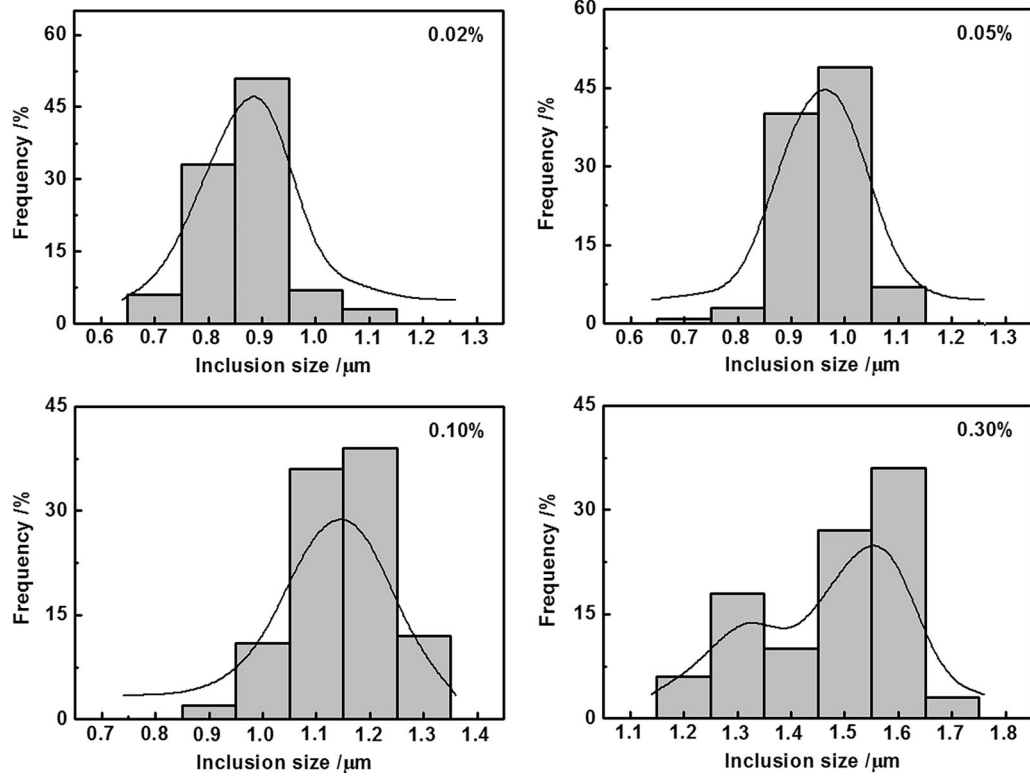


Fig. 10—Particle size distribution of inclusions in steel samples under the addition of different mass fractions of MgO nanoparticles.

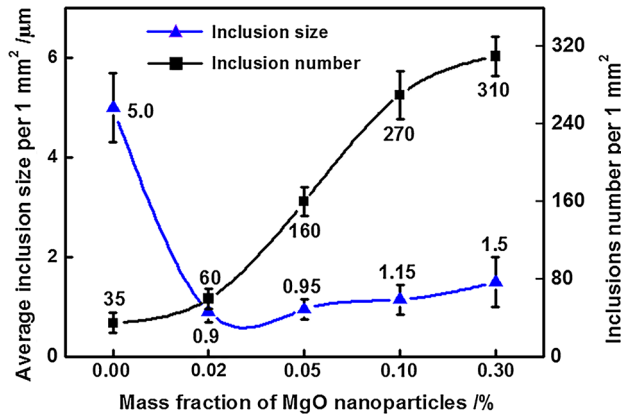


Fig. 11—Variation tendency of inclusion size and number per unit area (1 mm²) with the addition of different amounts of MgO nanoparticles.

According to the analysis method of Wang *et al.*,^[41] the model of intragranular ferrite formation on the surface of inclusions is adopted as illustrated in Figure 17, and both MgO-Al₂O₃-bearing hybrid inclusions and ferrite nucleus can be regarded as spherical. The inclusion size can be larger than the critical nucleus size or smaller. Initially, ferrite nucleation occurs at the interface between inclusion and parent phase.

1. Nucleation thermomechanical analysis

Based on the classical nucleation theory, the energy which needs to be overcome in the initial process of

nucleating and surpassing the critical nucleus size strictly depends on the location of nucleation. In general, this situation can be expressed by a factor, p :^[42]

$$p = \Delta G_I / \Delta G_H, \quad [1]$$

where ΔG_I and ΔG_H are the nuclear driving forces of ferrite formation on the surface of inclusion and homogeneous nucleation, respectively. p is an indicator that measures the difficulty of ferrite nucleation. The smaller the value of p , the easier the ferrite nucleation on the surface of inclusions. Through a series of formula iterations, the ultimate expression for the parameter p is deduced as follows:^[41]

$$p(R_I/r_c, \theta) = [2 - 3 \cos(\theta + \varphi) + \cos^3(\theta + \varphi)]/4 - (R_I/r_c^3)(2 - 3 \cos \varphi + \cos^3 \varphi)/4, \quad [2]$$

where R_I represents the radius of curvature of the inclusions, r_c is the critical nucleation radius of ferrite formation on the surface of inclusion, θ represents the contact angle between the ferrite and inclusion, and φ is a defined angle variable. It can be concluded from Eq. [2] that the value of p is mainly determined by two factors: the contact angle θ between critical nucleus and inclusion, and the inclusion size.

It is well known that there is a direct relationship between the value of contact angle θ and the interface between the inclusion and ferrite nucleus. To facilitate our investigation, in this study, the interfacial energy between any two among the inclusion, ferrite and austenite, is considered to be only related to their

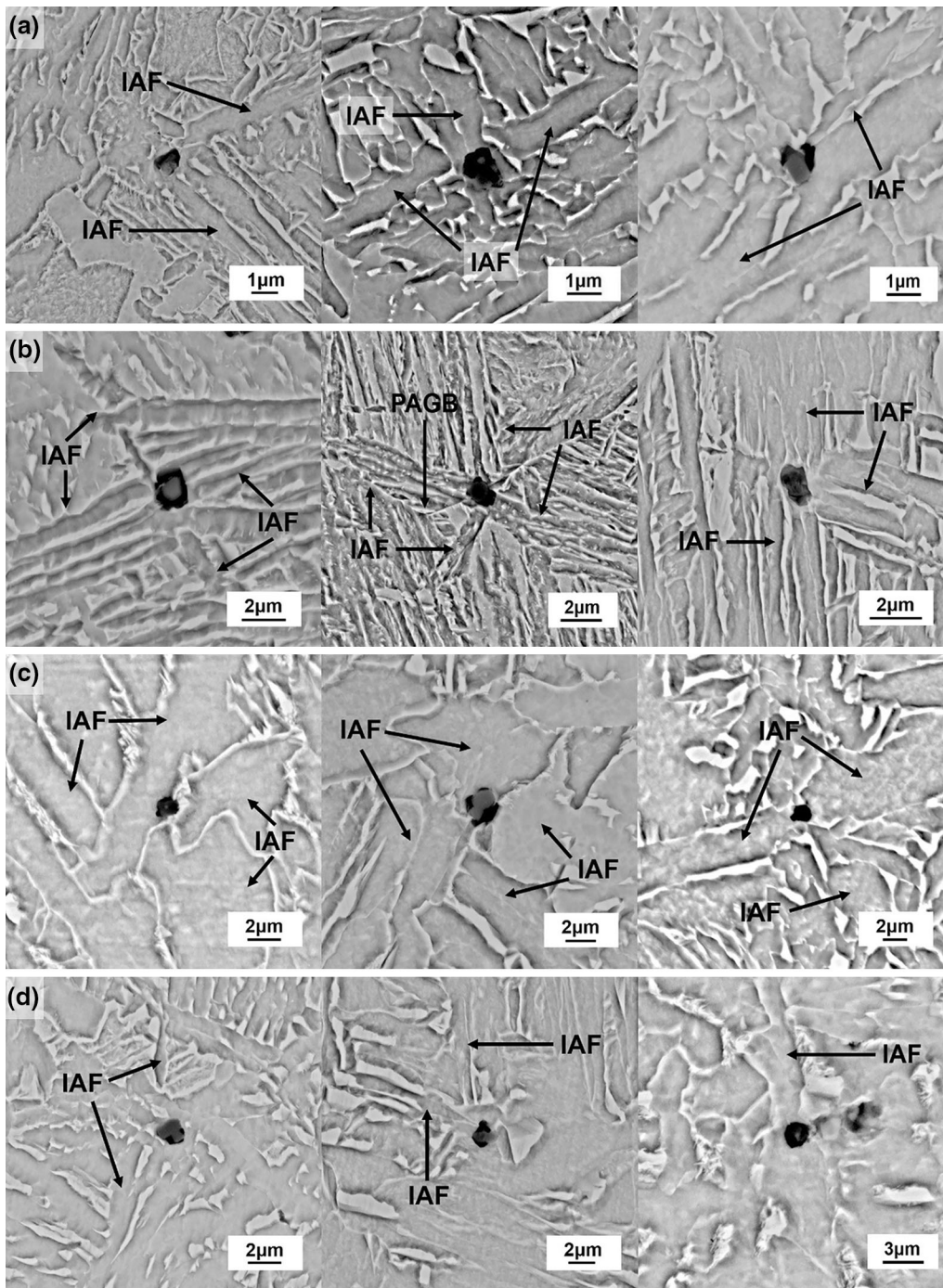


Fig. 12—Morphology of the AF induced by inclusions with increasing mass fraction of MgO nanoparticles.

respective characteristics. In this case, the inclusion characteristics mainly include crystal structure, chemical composition, and interfacial property between the inclusion and new phase. The inclusion size has no influence on these characteristics. Based on the above ideas, if only the inclusion type is determined, the inclusion characteristics should be constant and then the value of contact angle θ is also permanent. In this study, due to that MgO-Al₂O₃ is always the main part of the hybrid inclusions, the size of MgO-Al₂O₃-bearing hybrid inclusions is the decisive factor on the value of p .

Figure 18 shows the variation tendency of factor p with R_1/r_c at different contact angles θ .^[41] It can be recognized from Figure 18 that these curves have a common start and the value of p tends toward 1 with the value of R_1/r_c tending to 0, which indicates that the nucleation process tends toward homogeneous nucleation with increasing the value of R_1/r_c . For a constant contact angle θ in Figure 18, the value of p decreases sharply with increasing R_1/r_c in the initial stage of function curve, after which p tends toward a constant value. Overall, although larger inclusion size contributes to more ferrite nucleation, there

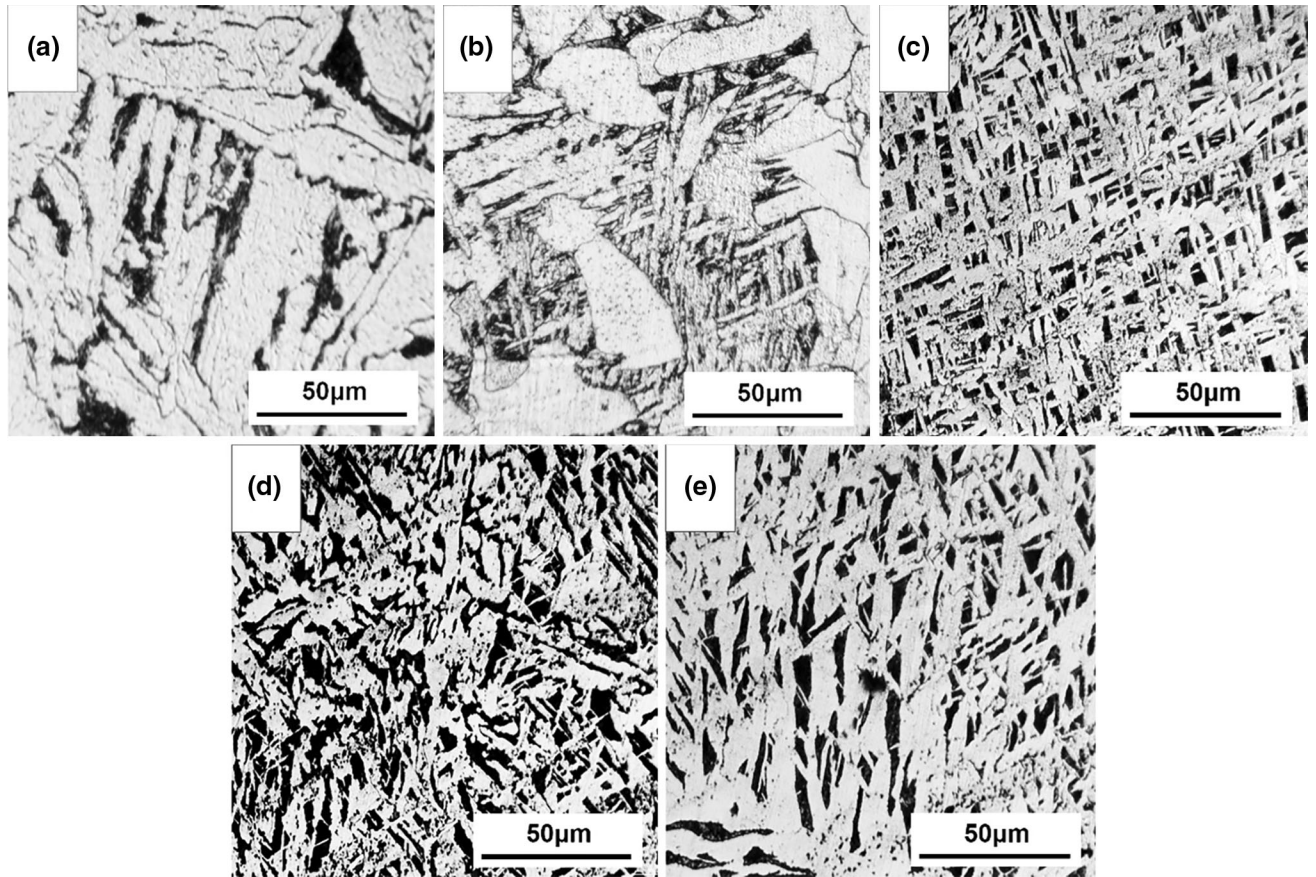


Fig. 13—Microstructural evolution of steel samples with increasing mass fractions of MgO nanoparticles: (a) 0.00 pct; (b) 0.02 pct; (c) 0.05 pct; (d) 0.10 pct; and (e) 0.30 pct.

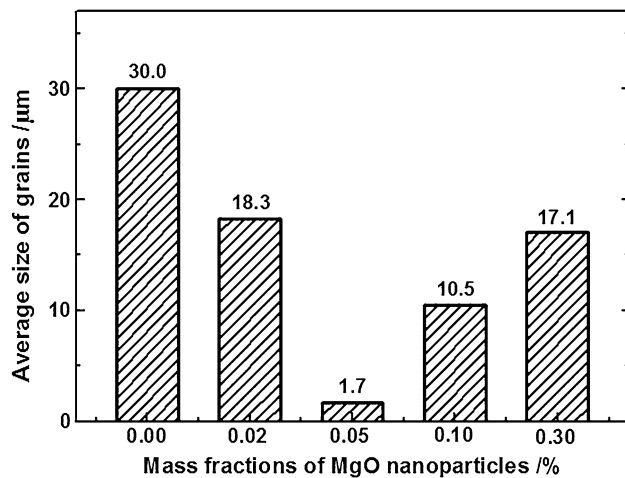


Fig. 14—Average grain size under the addition of different mass fractions of MgO nanoparticles.

is a critical size beyond which there will be little or no further influence on ferrite nucleation. Judging from Figure 18, the critical value R_1/r_c is about 50.

2. Nucleation dynamic analysis

The ferrite nucleation rate on the surface of inclusions expresses the number of ferrite nucleation in unit time

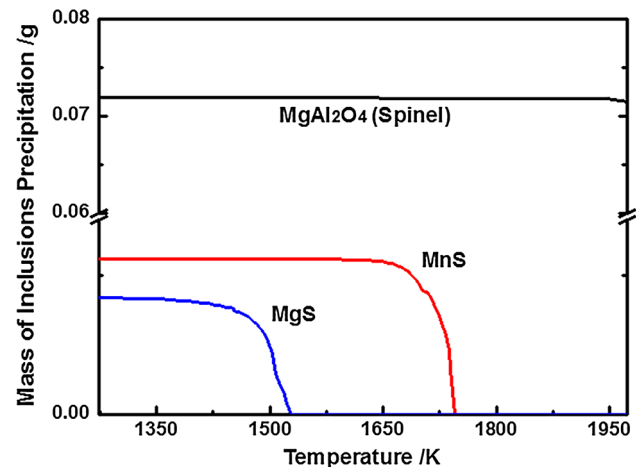


Fig. 15—Equilibrium precipitation of inclusions during solidification of Q235 steel with the addition of MgO nanoparticles.

and unit volume. It represents the nucleation speed and density which are the most basic concerns in actual production processes. Christian *et al.*^[43] deduced the following nucleation rate expression to explain the mechanism of ferrite nucleation on the surface of inclusions:

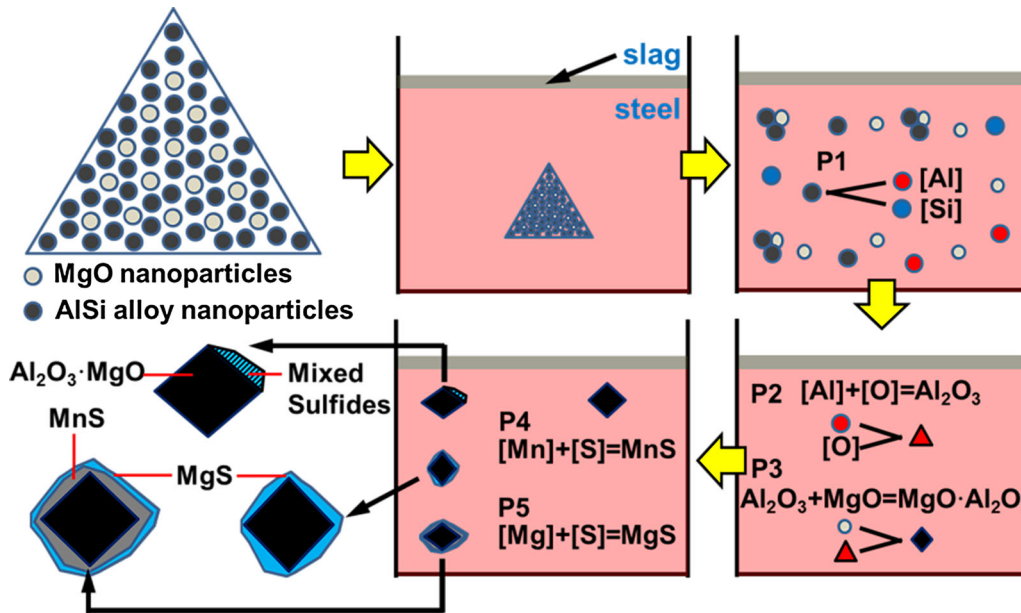


Fig. 16—Schematic diagram of inclusion precipitation behavior during the solidification of Q235 steel melt with the addition of nanoparticles.

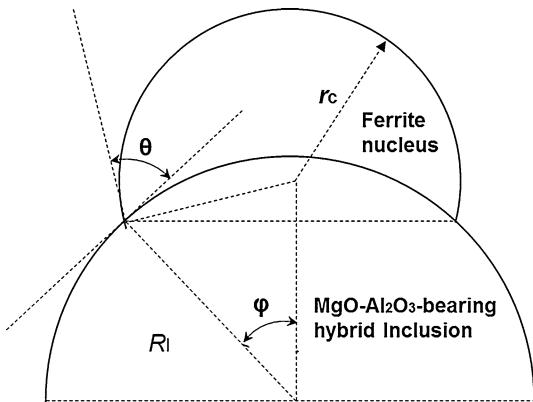


Fig. 17—Model of intragranular ferrite formation on the surface of inclusion.

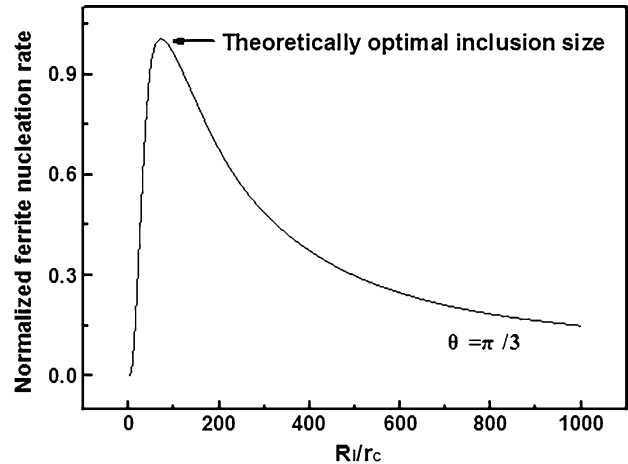


Fig. 19—Variation in the ferrite nucleation rate as a function of the inclusion size (R_i/r_c) for a contact angle θ of $\pi/3$.

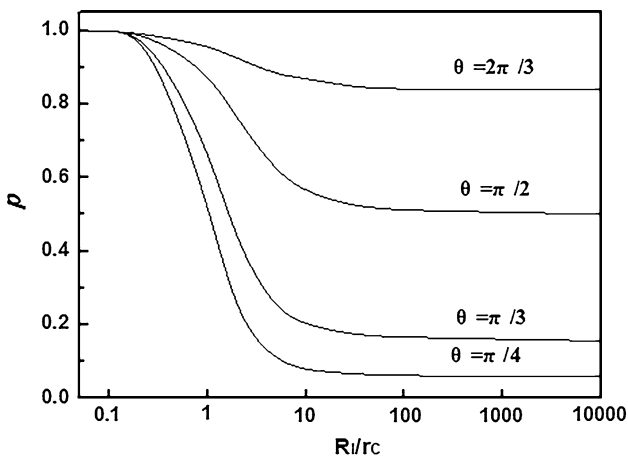


Fig. 18—Variation tendency of factor p with R_i/r_c at different contact angles θ .

$$I_I = f^* N_I \exp\left(-\frac{\Delta G_I + G_O}{k_B T}\right) \propto \frac{1}{R_I^3 (1 - \cos \varphi)} \cdot \exp\left[-\frac{p(R_I/r_c, \theta) \Delta G_H}{k_B T}\right], \quad [3]$$

where I_I is the ferrite nucleation rate, f^* is the transition frequency of Fe, N_I is the potential nucleation position of ferrite on the surface of inclusion, G_O is the grain boundary diffusion activation energy of Fe (4.72×10^{-19} J^[44]), k_B is the Boltzmann constant, and T is the absolute temperature.

Figure 19 shows the variation in the ferrite nucleation rate as a function of the inclusion size (R_i/r_c) for a contact angle θ of $\pi/3$. There exists a theoretically optimal inclusion size, and only within this range the

inclusions have a relatively large ferrite nucleation rate. Namely, the increase in the inclusion size, on one hand, decreases the value of p and increases the ferrite nucleation rate, and, on the other hand, it decreases the surface area of inclusion per unit volume and the ferrite nucleation rate. According to Eq. [3], when the inclusion size is a certain value, the increasing value of the exponential term caused by the decrease in p just compensates for the decrease in the effective nucleation area. The critical value is just the optimal inclusion size as shown in Figure 19.

3. Verification of results

Zhang and Thomas^[45] indicated that the contact angle θ between MgO and Al₂O₃ inclusion and liquid steel is 118-136 and 134-146 deg, respectively. Previous studies^[46,47] also showed that compared with the pure inclusion, hybrid inclusion induces ferrite more easily due to the relatively higher misfit between the structures of hybrid inclusion and austenite. Although it can be deduced that the contact angle θ between the MgO-Al₂O₃-bearing hybrid inclusions and steel melt is smaller than any one of the above two pure inclusions, the exact value is not clear. Offerman *et al.*^[48] confirmed that the critical nucleus size of ferrite should be in the range of 0.71-1.56 nm. Based on the critical inclusion size observed in Figure 18 and the inclusion size range corresponding to the largest ferrite nucleation rate in Figure 19, assuming that the range of R_1/r_c is 100-300, the following formula is workable: $2R_1 = (200-600)r_c$. That is to say, the size range of inclusions which can facilitate ferrite formation is 0.142 to 0.936 μm . According to the experimental results and analyses in Section III, the optimal inclusion size contributing to facilitating ferrite formation can be confirmed to be about 0.950 μm . Thus, the experimental results and the conclusion of nucleation analysis are basically in good agreement.

C. Microstructure

In addition to the inclusion type, the main factors that determine the grain refining effect are the inclusion size and inclusion density. Overall, the microstructure becomes finer gradually with increasing amounts of MgO addition from 0.05 to 0.3 wt pct as shown in Figure 14. With the addition of 0.02 wt pct MgO nanoparticles, although the average size of inclusions becomes smaller compared with that of the steel without the addition of nanoparticles, the amount of inclusions per unit area is much less than that of the other test steels with the addition of MgO nanoparticles with the mass fraction of 0.05 to 0.3 wt pct. As a result, some fine AFs appear while the coarse ferrites are still the primary microstructural feature. When the addition amounts of MgO nanoparticles increase to 0.05 wt pct, the aggregation phenomenon between individual particles is not obvious and the inclusions induce more fine AF. This is the reason why the average grain size of microstructure in the latter case is finer than that in the former. When the addition amounts of MgO nanoparticles increase to 0.1 or 0.3 wt pct, the aggregation phenomenon between

individual particles tends to be serious gradually, which ultimately results in a decline in the ability of inclusions to induce AF.

V. SUMMARY AND CONCLUSION

After adding MgO nanoparticles pre-dispersed with AlSi alloy nanoparticles to Q235 steel, the majority of the reaction products were MgO·Al₂O₃ spinel and MgO-Al₂O₃-bearing hybrid inclusions. With the mass fraction of MgO nanoparticles increasing from 0.02 to 0.05, 0.1, and 0.3 pct, the average size of inclusions was 0.90, 0.95, 1.15, and 1.5 μm respectively. These inclusions were significantly smaller than those found in steel without the addition of MgO nanoparticles, where the average inclusion size was 5.0 μm . With the addition of increasing amounts of MgO, the aggregation phenomenon between individual particles tended to be more serious.

After adding MgO nanoparticles to Q235 steel, the majority of formed inclusions have a good ability for inducing AF formation. When the mass fraction of MgO nanoparticles in steel increased from 0.02 to 0.05 pct, the proportion of AF in the steel microstructure increased progressively. With increasing the addition amounts of MgO to 0.1 and 0.3 wt pct, only few of the inclusions could induce AF formation and the inducing ability of inclusions for AF greatly declined. This mainly results from the value of the ferrite nucleation rate which is relatively high only within a small range of inclusion size.

When the addition amount of MgO nanoparticles was 0.05 wt pct, the proportion of AF in the microstructure is relatively larger and the degree of interlocking of the AF within the microstructure was optimized. The ferrite grains also got refined and the average grain size decreased by more than 94 pct compared with that of the original steel.

ACKNOWLEDGMENTS

This research is supported by the National Science Foundation of China (No. 51374021 and 51304016).

NOMENCLATURE

AF	Acicular ferrite
EAM	External addition method
EDS	Energy-dispersive spectrometry
f^*	Transition frequency of Fe
φ	Defined angle variables
ΔG_H	Nuclear driving forces of ferrite formation in homogeneous nucleation
ΔG_I	Nuclear driving forces of ferrite formation on the surface of inclusion
G_O	Grain boundary diffusion activation energy of Fe

I_1	Ferrite nucleation rate
IAF	Intragranular acicular ferrite
IPM	Internal precipitation method
k_B	Boltzmann constant
N_1	Potential nucleation position of ferrite on the surface of inclusion
p	An indicator that measures the difficulty of ferrite nucleation
PAGB	Prior austenite grain boundaries
r_c	Critical nucleation radius of ferrite formation on the surface of inclusion
R_1	Radius of curvature of the inclusions
SEM	Scanning electron microscopy
T	Absolute temperature
θ	Contact angle between ferrite and inclusion

REFERENCES

- D.L. Liu, Y.L. Wang, X.D. Huo, N.J. Cheng, W.R. Shao, J. Fu, and Y.L. Yong: *Acta Metall. Sin.*, 2002, vol. 38, pp. 647–54 (in Chinese).
- M. Niikura, M. Fujioka, Y. Adachi, A. Matsukura, T. Yokota, Y. Shirota, and Y. Hagiwara: *J. Mater. Process. Technol.*, 2001, vol. 117, pp. 341–46.
- P. Cizek, B. Wynne, C. Davies, B. Muddle, and P. Hodgson: *Metall. Mater. Trans. A*, 2002, vol. 33A, pp. 1331–49.
- A. Kojima, Y. Watanabe, Y. Terada, A. Yoshie, and H. Tamehiro: *ISIJ Int.*, 1996, vol. 35, pp. 603–10.
- H. Beladi, G.L. Kelly, A. Shokouhi, and P.D. Hodgson: *Mater. Sci. Eng. A Struct.*, 2004, vol. 371, pp. 343–52.
- P.C.M. Rodrigues, E.V. Pereloma, and D.B. Santos: *Mater. Sci. Eng. A Struct.*, 2000, vol. 283, pp. 136–43.
- X.B. Li, M. Yi, C.J. Liu, and M.F. Jiang: *Steel Res. Int.*, 2015, vol. 85, pp. 1–11.
- C. Zener: *Trans. Am. Inst. Metall. Eng.*, 1949, vol. 175, pp. 15–17.
- P.L. Harrison and R.A. Farrar: *J. Mater. Sci.*, 1981, vol. 16, pp. 2218–26.
- J. Takamura, and S. Mizoguchi: *Proceedings of 6th International Iron and Steel Congress.*, Iron and Steel Institution Japan, Tokyo, 1990, pp. 591–95.
- S. Mizoguchi, and J. Takamura: *Proceedings of 6th International Iron and Steel Congress.*, Iron and Steel Institution Japan, Tokyo, 1990, pp. 598–604.
- J.S. Byun, J.H. Shim, Y.W. Chou, and D.N. Lee: *Acta Mater.*, 2003, vol. 51, pp. 1593–1606.
- H. Homma, S. Ohkita, S. Matsuda, and K. Yamamoto: *Weld J.*, 1987, vol. 66, pp. 301–09.
- K. Yamamoto, T. Hasegawa, and J. Takamura: *ISIJ Int.*, 1996, vol. 36, pp. 80–86.
- D.L. Shang and C.F. Lv: *Chin. J. Eng.*, 2008, vol. 30, pp. 864–69 (in Chinese).
- D.L. Shang, D.G. Li, C.F. Lv, L. Kang, and W. Deng: *Chin. J. Eng.*, 2010, vol. 32, pp. 1418–21 (in Chinese).
- S.S. Babu and S.A. David: *ISIJ Int.*, 2002, vol. 42, pp. 1344–53.
- S. Talas and R.C. Cochrane: *J. Alloys Compd.*, 2005, vol. 396, pp. 224–27.
- R.A. Ricks, P.R. Howell, and G.S. Barritte: *J. Mater. Sci.*, 1982, vol. 17, pp. 732–40.
- M.I. Vega, S.F. Medina, A. Quispec, M. Gómezb, and P.P. Gómez: *Mater. Sci. Eng. A Struct.*, 2006, vol. 423, pp. 253–61.
- Z.T. Ma and D. Janke: *Acta Metall. Sin. Engl.*, 2009, vol. 11, pp. 79–86.
- A.M. Guo, S.R. Li, J. Guo, P.H. Li, Q.F. Ding, K.M. Wu, and X.L. He: *Mater. Charact.*, 2008, vol. 59, pp. 134–39.
- O. Grong, L. Kolbeinsen, C. van der Eijk, and G. Tranell: *ISIJ Int.*, 2006, vol. 46, pp. 824–31.
- K. Nishioka and K. Ichikawa: *Sci. Technol. Adv. Mater.*, 2012, vol. 13, pp. 1–20.
- M. Hasegawa and K. Takeshita: *Metall. Mater. Trans. B*, 1978, vol. 09B, pp. 383–88.
- J.M. Gregg and H.K.D.H. Bhadeshia: *Acta Mater.*, 1997, vol. 45, pp. 739–48.
- G.C. Wang, T.M. Wang, S.N. Li, and K.M. Fang: *Chin. J. Eng.*, 2007, vol. 29, pp. 578–81 (in Chinese).
- Z.D. Huang, J.P. Niu, Q.K. Cai, and L. Wang: *J. Northeast. Univ.*, 2009, vol. 30, pp. 997–1000 (in Chinese).
- B. Wen and B. Song: *Steel Res. Int.*, 2012, vol. 83, pp. 487–95.
- Y.F. Liang, J.P. Lin, F. Ye, Y.J. Li, Y.L. Wang, and G.L. Chen: *J. Alloys Compd.*, 2010, vol. 504, pp. S476–79.
- J.H. Shim, Y.W. Cho, J.D. Shim, and D.N. Lee: *Metall. Mater. Trans. B*, 2000, vol. 32B, pp. 75–83.
- H.S. Kim, H.G. Lee, and K.S. Oh: *Met. Mater.*, 2000, vol. 06, pp. 305–10.
- S.F. Yang, Q.Q. Wang, L.F. Zhang, J.S. Li, and Kent. Peaslee: *Metall. Mater. Trans. B*, 2012, vol. 43B, pp. 731–50.
- J.H. Park: *Metall. Mater. Trans. B*, 2007, vol. 38B, pp. 657–63.
- K. Fujii, T. Nagasaka, and M. Hino: *ISIJ Int.*, 2000, vol. 40, pp. 1059–66.
- C.W. Seo, S.H. Kim, S.K. Jo, M.O. Suk, and S.M. Byun: *Metall. Mater. Trans. B*, 2010, vol. 41B, pp. 790–97.
- S.K. Jo, S.H. Kim, and B. Song: *Metall. Mater. Trans. B*, 2002, vol. 33B, pp. 703–09.
- K.P. Wang, M. Jiang, X.H. Wang, Y. Wang, H.Q. Zhao, and Z.M. Cao: *Metall. Mater. Trans. B*, 2015, vol. 46, pp. 2198–2207.
- M. Wakoh, T. Sawai, and S. Mizoguchi: *ISIJ Int.*, 1996, vol. 36, pp. 1014–21.
- B. Wen, B. Song, N. Pan, Q.Y. Hu, and J.H. Mao: *Ironmak. Steelmak.*, 2011, vol. 38, pp. 577–83.
- W. Wang and L.M. Fu: *Acta Metall. Sin.*, 2008, vol. 06, pp. 723–28 (in Chinese).
- J.W. Christian: *The Theory of Transformation in Metals and Alloys*, Pergamon Press, Oxford, 1975, pp. 1–20.
- J.W. Christian: in *Physical Metallurgy*, R.W. Cahn, ed., North-Holland Publishing Company, Amsterdam, 1977, 1st Ed., pp. 479–580.
- P.J. Clemm and J.C. Fisher: *Acta Metall.*, 1955, vol. 03, pp. 70–73.
- L.F. Zhang, and B.G. Thomas: *XXIV National Steelmaking Symposium*, Morelia, Mich, Mexico, 2005, vol. 02, pp. 138–83.
- A.R. Mills, G. Thewlis, and J.A. Whiteman: *Mater. Sci. Technol.*, 1987, vol. 03, pp. 1051–61.
- J.L. Lee and Y.T. Pan: *ISIJ Int.*, 1995, vol. 35, pp. 1027–34.
- S.E. Offerman, N.H. Van Dijk, J. Sietsma, S. Van Der Zwaag, E.M. Lauridsen, L. Margulies, S. Grigull, and H.F. Poulsen: *Science*, 2002, vol. 298, pp. 1003–05.